



This is a repository copy of *Fatigue resistant lead-free multilayer ceramic capacitors with ultrahigh energy density*.

White Rose Research Online URL for this paper:  
<https://eprints.whiterose.ac.uk/160994/>

Version: Published Version

---

**Article:**

Wang, G., Lu, Z., Yang, H. et al. (9 more authors) (2020) Fatigue resistant lead-free multilayer ceramic capacitors with ultrahigh energy density. *Journal of Materials Chemistry A*, 8 (22). pp. 11414-11423. ISSN 2050-7488

<https://doi.org/10.1039/d0ta00216j>

---

**Reuse**

This article is distributed under the terms of the Creative Commons Attribution (CC BY) licence. This licence allows you to distribute, remix, tweak, and build upon the work, even commercially, as long as you credit the authors for the original work. More information and the full terms of the licence here:  
<https://creativecommons.org/licenses/>

**Takedown**

If you consider content in White Rose Research Online to be in breach of UK law, please notify us by emailing [eprints@whiterose.ac.uk](mailto:eprints@whiterose.ac.uk) including the URL of the record and the reason for the withdrawal request.



[eprints@whiterose.ac.uk](mailto:eprints@whiterose.ac.uk)  
<https://eprints.whiterose.ac.uk/>

# Journal of Materials Chemistry A

Materials for energy and sustainability

Accepted Manuscript

This article can be cited before page numbers have been issued, to do this please use: G. Wang, Z. Lu, H. Yang, H. Ji, A. Mostaed, L. li, Y. wei, A. Feteira, S. Sun, D. Wang, D. Sinclair and I. M. Reaney, *J. Mater. Chem. A*, 2020, DOI: 10.1039/D0TA00216J.



This is an Accepted Manuscript, which has been through the Royal Society of Chemistry peer review process and has been accepted for publication.

Accepted Manuscripts are published online shortly after acceptance, before technical editing, formatting and proof reading. Using this free service, authors can make their results available to the community, in citable form, before we publish the edited article. We will replace this Accepted Manuscript with the edited and formatted Advance Article as soon as it is available.

You can find more information about Accepted Manuscripts in the [Information for Authors](#).

Please note that technical editing may introduce minor changes to the text and/or graphics, which may alter content. The journal's standard [Terms & Conditions](#) and the [Ethical guidelines](#) still apply. In no event shall the Royal Society of Chemistry be held responsible for any errors or omissions in this Accepted Manuscript or any consequences arising from the use of any information it contains.

# Fatigue resistant lead-free multilayer ceramic capacitors with ultrahigh energy density

View Article Online

DOI: 10.1039/C9JA00216J

Ge Wang<sup>a#</sup>, Zhilun Lu<sup>ab#</sup>, Huijing Yang<sup>a,c#</sup>, Hongfen Ji<sup>a,d#</sup>, Ali Mostaed<sup>a</sup>, Linhao Li<sup>a</sup>, Yiqi Wei<sup>a</sup>, Antonio Feteira<sup>e</sup>, Shikuan Sun<sup>a</sup>, Derek C. Sinclair<sup>a</sup>, Dawei Wang<sup>a\*</sup>, Ian M. Reaney<sup>a</sup>

<sup>a</sup>Department of Materials Science and Engineering, University of Sheffield, Sheffield S1 3JD, UK

<sup>b</sup>The Henry Royce Institute, Sir Robert Hadfield Building, Sheffield, S1 3JD, UK

<sup>c</sup>Department of Physics, Tangshan Normal University, Tangshan 063000, China

<sup>d</sup>Laboratory of Thin Film Techniques and Optical Test, Xi'an Technological University, Xi'an 710032, China

<sup>e</sup>Christian Doppler Laboratory for Advanced Ferroic Oxides, Sheffield Hallam University, Sheffield S1 1WB, UK

\*Corresponding author. E-mail address: dawei.wang@sheffield.ac.uk

#Author Contributions: G.W., Z.L. H.Y. and H.J. contributed equally to this work and should be considered as co-first authors.

## Abstract

The critical role of electrical homogeneity in optimising electric-field breakdown strength (BDS) and energy storage in high energy density  $(0.7-x)\text{BiFeO}_3-0.3\text{BaTiO}_3-x\text{Bi}(\text{Li}_{0.5}\text{Nb}_{0.5})\text{O}_3$  (BF-BT-xBLN) lead-free capacitors is demonstrated. The high BDS for bulk ceramics and multilayers (dielectric layer thickness  $\sim 8 \mu\text{m}$ ) of  $\sim 260$  and  $\sim 950 \text{ kV cm}^{-1}$ , respectively, gives rise to record-performance of recoverable energy density,  $W_{\text{rec}} = 13.8 \text{ J cm}^{-3}$  and efficiency,  $\eta = 81\%$ . Under an electric field of  $400 \text{ kV cm}^{-1}$ , multilayers are temperature stable up to  $100 \text{ }^\circ\text{C}$ , frequency independent in the range  $10^{-2}$  to  $10^2 \text{ Hz}$ , have low strain ( $< 0.03\%$ ) and are fatigue-resistant up to  $10^4$  cycles ( $W_{\text{rec}}$  variation  $< 10\%$ ). These properties show promise for practical use in pulsed power systems.

**Keywords:** energy storage; multilayer ceramic capacitors; bismuth ferrite; lead-free; fatigue-resistant



## Introduction

View Article Online  
DOI: 10.1039/D0TA00216J

The depletion of fossil fuel reserves and serious concerns over climate change have provoked the development of renewable energy including tidal, wind and solar. [1-5] Electrical energy is currently stored or generated autonomously through a range of devices such as fuel cells and batteries. [1-3, 6-13] For energy storage applications, dielectric capacitors have the advantages of fast charging-discharging speed, superior temperature stability and are mainly used for pulsed power applications such as power distribution, medical transportation devices and pulsed power weapons. [4-5, 14-18]. Dielectric polymers are limited by their low melting temperatures and related degradation [1, 2]. Dielectric ceramics are potentially more temperature stable than dielectric polymers but have comparatively low recoverable energy density ( $W_{rec}$ ) and energy conversion efficiency ( $\eta$ ), due to their low electric-field breakdown strength (BDS) and high energy loss ( $W_{loss}$ ).

To satisfy the requirements of power supply components in portable electronics, electric vehicles and other high power and energy storage applications, both high  $W_{rec}$  and  $\eta$  are required. For dielectric capacitors, the total energy density ( $W$ ),  $W_{rec}$  and  $\eta$  are given by:

$$W = \int_0^{P_{max}} E dP, \quad (1)$$

$$W_{rec} = \int_{P_r}^{P_{max}} E dP, \quad (2)$$

$$\eta = W_{rec}/W \quad (3)$$

where  $P$ ,  $P_{max}$  and  $P_r$  are the polarization, maximum polarization and remanent polarisation, respectively. A high BDS, combined with large  $P_{max}$  and small  $P_r$  are simultaneously desirable to achieve both high  $W_{rec}$  and  $\eta$ . Furthermore, the stability and fatigue resistant of materials and devices over a range of temperature and frequency are critical. [19-22]

Although high energy storage performance with  $W_{rec} \sim 10.4 \text{ J cm}^{-3}$  and a  $\eta \sim 87\%$  has been achieved with La and Sn co-doped lead zirconate at  $400 \text{ kV cm}^{-1}$ , [23] lead-free ceramics based on  $\text{AgNbO}_3$  (AN),  $\text{BaTiO}_3$  (BT),  $(\text{Bi}_{0.5}\text{Na}_{0.5})\text{TiO}_3$  (BNT),  $(\text{K}_{0.5}\text{Na}_{0.5})\text{NbO}_3$  (KNN) and  $\text{BiFeO}_3$ - $\text{BaTiO}_3$  (BF-BT) have all been studied due to concerns over the toxicity of lead. [24-56] High  $W_{rec}$  ( $> 3 \text{ J cm}^{-3}$ ) has been reported in antiferroelectric (AFE) (Ta, La and Gd)-doped AN with enhanced BDS up to  $300 \text{ kV cm}^{-1}$ . [24-28] Oxide additives ( $\text{Al}_2\text{O}_3$ ,  $\text{SiO}_2$ ,  $\text{MgO}$ ) and  $\text{Bi(A,B)O}_3$  ( $A = \text{Li, Mg and Zn}$ ,  $B = \text{Nb, Ta, Ti and Zr}$ ) have all been found to improve  $W_{rec}$  and BDS of BT-based ceramics up to  $2.9 \text{ J cm}^{-3}$  and  $300 \text{ kV cm}^{-1}$ , respectively. [29-36] Recently,  $W_{rec} \sim 7 \text{ J cm}^{-3}$  with high  $\eta \sim 85\%$  was reported in  $\text{NaNbO}_3$ -doped BNT [37] at  $390 \text{ kV cm}^{-1}$  and  $W_{rec} \sim 4 \text{ J cm}^{-3}$  were also obtained for KNN-based ceramics due to enhancement of BDS ( $300\sim 400 \text{ kV cm}^{-1}$ ) by controlled grain growth. [46-49]

(1-x)BF-xBT materials initially drew attention as potential lead-free piezoelectrics with high piezoelectric coefficient ( $d_{33}$ ) $\sim 402 \text{ pC N}^{-1}$ , normalised strain ( $d_{33}^*$ ) $\sim 600 \text{ pm V}^{-1}$  and Curie temperature



( $T_c$ ) ~ 454 °C in a mixed-phase region of rhombohedral and pseudocubic with  $x=0.25$  to  $0.35$ .<sup>[57, 58]</sup> The mixture of highly polarisable ions such as  $\text{Bi}^{3+}$  and  $\text{Ti}^{4+}$  in a matrix of dissimilar sized  $\text{ABO}_3$ , perovskite unit cells is considered responsible for its strong piezoelectric/electrostrictive response.<sup>[59]</sup> These crystallo-chemical features are also considered ideal for optimising polarisation within a pseudocubic relaxor phase and thus provide a base from which to devise materials with high energy density. For example, BF-BT based compositions with various dopants such as Nd and  $\text{A}(\text{B}_1, \text{B}_2)\text{O}_3$  ( $\text{A}=\text{Bi}$  and Nd,  $\text{B}_1=\text{Zn}$  and Mg,  $\text{B}_2=\text{Nb}$  and Zr),<sup>[50-56]</sup> have all been shown to exhibit high energy density. The best compositions to date however, are doped with  $\text{Nd}(\text{Zn}_{1/2}\text{Zr}_{1/2})\text{O}_3$  and give  $W_{rec} \sim 2.5 \text{ J cm}^{-3}$  with  $\text{BDS} > 260 \text{ kV cm}^{-1}$  for ceramics which improve dramatically when multilayered to  $10.5 \text{ J cm}^{-3}$  at  $700 \text{ kV cm}^{-1}$ .<sup>[56]</sup>

Enhancement of BDS in dielectric materials is an effective approach to optimize  $W_{rec}$ , and is associated with factors such as the band gap, reduced porosity, grain size, impurity concentrations, sample thickness/geometry and space-charging polarization.<sup>[60]</sup> However, practically, BDS is limited in many materials by the presence of conductive pathways, e.g. from core to core or from shell to shell, which appear as electrical inhomogeneity in impedance spectroscopy (IS) data.<sup>[61-63]</sup>

The relationship between BDS and dielectric layer thickness was first published by Gerson and Marshall in 1959.<sup>[64]</sup> In principle, all solid dielectrics increase their BDS with decreasing layer thickness, culminating in values of  $>1 \text{ MV cm}^{-1}$  for thin films.<sup>[65]</sup> In our own research, we have demonstrated this effect numerous times, as have several research groups, by fabricating multilayer capacitors (10  $\mu\text{m}$  dielectric layer thickness) once good properties (high resistivity and electrical homogeneity) have been demonstrated in bulk ceramics.<sup>[51, 56]</sup> However, with any given multilayer, short circuit pathways can emerge between low resistivity regions as layer thickness decreases, thereby decreasing BDS. The caveat therefore, which must be applied to the Gerson and Marshall<sup>[64]</sup> relationship is that BDS will only increase if low resistivity pathways are eliminated, i.e. the materials have a high resistivity and are electrically homogeneous.

In this study, we utilise stoichiometric doping, the nature of which is complex but which has been dealt with by Sinclair and co-workers for several systems, e.g. BNT-based,<sup>[66-68]</sup> and BF-BT-based<sup>[69-71]</sup> materials. Stoichiometric doping has been shown to be effective at reducing conductivity and promoting electrical homogeneity in a wide range of systems.<sup>[50, 56, 67, 68]</sup> By eliminating extrinsic effects through electrical homogeneity, we enable the Gerson and Marshall effect (Figure 1), resulting in  $W_{rec} \sim 13.8 \text{ J cm}^{-3}$  at  $\sim 950 \text{ kV cm}^{-1}$  in 0.57BF-0.30BT-0.13BLN ceramic multilayers. Furthermore, excellent fatigue properties with respect to temperature, frequency and cyclic poling are demonstrated which play a critical role in practical applications.



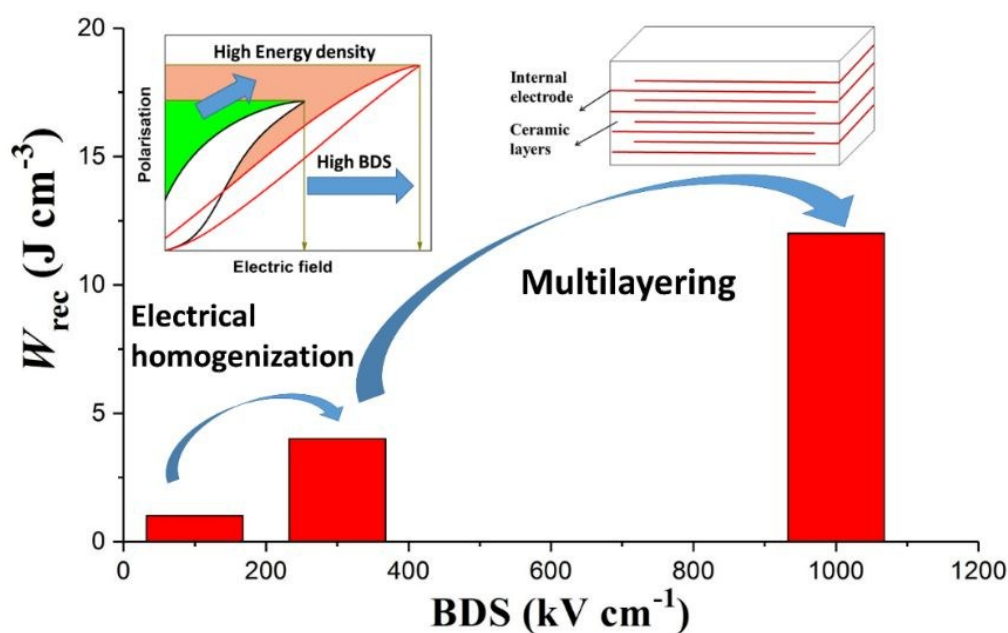


Figure 1. Schematic figure of optimizing BDS and energy storage properties by electrical homogenization and multilayering.

## Results and Discussion

### High energy density dielectric ceramics

The crystal structure of crushed BF-BT-xBLN ceramics ( $0.00 \leq x \leq 0.15$ ) was determined using XRD, as shown in Figure 2(a). XRD patterns are indexed as a single-phase perovskite phase without any detectable secondary impurity phases for  $x < 0.08$ . Impurity peaks are observed for  $x \geq 0.08$  at which point in the composition, the solid solubility limit of  $\text{Li}_{0.5}\text{Nb}_{0.5}$  on the B-site of BF-BT is exceeded. The average ionic radii ( $R$ ) of  $(\text{Li}_{0.5}\text{Nb}_{0.5})^{3+}$  ions are given by  $R = 0.5R(\text{Li}^+) + 0.5R(\text{Nb}^{5+}) = 0.70 \text{ \AA}$  ( $0.76 \text{ \AA}$  and  $0.64 \text{ \AA}$  are the respective ionic radii of  $\text{Li}^+$  and  $\text{Nb}^{5+}$  in six-fold coordination), which is larger than that of  $\text{Fe}^{3+}$  and  $\text{Ti}^{4+}$  ( $0.645$  and  $0.605 \text{ \AA}$ , respectively) in the same co-ordination.<sup>[72]</sup> As  $x$  increases therefore, diffraction peaks shift left, commensurate with an increase in lattice parameter (Figure S1, Electronic Supplementary material). A full-pattern Rietveld refinement on XRD data for BF-BT-0.13BLN ceramics has been conducted using TOPAS 5. The best fitting was obtained using a mixed-phase assemblage of  $R3c$  Rhombohedral (14%) and  $Pm3m$  Cubic phase (86%), as displayed in Figure S2 (Electronic Supplementary Information) and Table S1 (Electronic Supplementary Information), consistent with previous reports on BF-BT ternary systems.<sup>[50, 51, 56, 76, 73]</sup>

The temperature-dependent permittivity ( $\epsilon_r$  vs  $T$ ) and dielectric loss ( $\tan \delta$  vs  $T$ ) data at 100 kHz for BF-BT-xBLN ceramics are presented in Figure 2(b). A single sharp peak at a  $T_c$  of  $\sim 480 \text{ }^\circ\text{C}$  is observed for undoped BF-BT, associated with a ferroelectric to paraelectric transition. As the BLN concentration



increases, the dielectric maxima broadens, accompanied by a lowering of the maximum value of  $\epsilon_r$ . Broad frequency-dependent  $\epsilon_r$ -T peaks are obtained for compositions with  $x > 0.02$ , as displayed in Figure S3 (Electronic Supplementary Information), indicating a compositionally driven transition from dominantly ferroelectric to relaxor behaviour. Despite these changes, low values of  $\tan \delta$  are recorded in all samples below 250 °C but increase substantially above this temperature. There is however, no systematic trend in the dielectric loss above 250 °C with increasing  $x$ . There will be increasing contributions from space charge (long range conduction) to the loss but bulk conductivity values obtained from impedance spectroscopy data do not support a simple hypothesis of increasing oxygen vacancies with BLN content, as illustrated in Figure S4 (Electronic Supplementary Information). In fact, the bulk conductivity is lower in  $x = 0.15$  than it is for lower  $x$  values.

The activation energy for total conductivity (Figure S4, Electronic Supplementary Information) remains broadly the same for all compositions suggesting that the conduction mechanism (but not necessarily) conductivity remains the same as dopant concentration increases. Conductivity remains via  $V_O$  diffusion throughout consistent with an activation energy of  $\sim 1.1$ - $1.2$  eV and points to substitution/compensation in accordance with the batched stoichiometry.<sup>[67]</sup> However, the site location of Li may locally play a role in the defect chemistry and is an area of future work.

From Figure 2b,  $x = 0$  shows classic paraelectric behaviour above  $T_c$  at 480 °C whereas with increasing  $x$ ,  $\epsilon_r$  in the range 480 - 600 °C broadens and becomes relaxor-like. As a consequence, a significant contribution to the loss must still be associated with polarisation rotation/coalescence of polar nano regions (relaxor behaviour) at higher values of  $x$ . Polarization-electric field (P-E) loops obtained at 100 kV cm<sup>-1</sup> for BF-BT-xBLN ceramics are displayed in Figure 2(c). The highest polarization values are recorded for undoped BF-BT with  $P_{max} \sim 34$   $\mu\text{C cm}^{-2}$  and  $P_r \sim 25$   $\mu\text{C cm}^{-2}$ . P-E loops become slimmer and are no longer saturated as the BLN concentration increases, along with a continuous reduction of  $P_m$ ,  $P_r$  and  $E_C$  (Figure S5, Electronic Supplementary Information), typical of a transition from ferroelectric to relaxor behaviour.

The SE and BSE images for BF-BT-xBLN ceramics are displayed in Figure S6 and S7 (Electronic Supplementary Information). The largest grain size ( $\sim 8$   $\mu\text{m}$ ) is observed for undoped BF-BT. For BLN-doped compositions, the grain size reduces significantly (Figure S6 and S7, Electronic Supplementary Information) accompanied by the formation of a core-shell microstructure, exhibiting Bi/Fe-rich (bright), Ba-rich (dark) regions and Bi-rich (bright GB phase), Figure 2d and Table S2 (Electronic Supplementary Information). The bright grain boundary phase is Bi-rich, consistent with impurity peaks in XRD pattern.

The formation of the core-shell structure is driven by immiscibility of the perovskite end members which not only have dissimilar ion size, e.g.  $\text{Ba}^{2+} \gg \text{Bi}^{3+}$  but have different bonding with  $\text{Bi}^{3+}$  being dominantly covalent whereas  $\text{Ba}^{2+}$  is considered ionic. Immiscibility in part can be suppressed by quenching and



by careful selection of dopants. [70, 71, 74-76] The core-shell structure in BF-BT-0.13BLN ceramics is investigated further by TEM (Figure S8, Electronic supplementary information) and exhibits small tweed domains (Core) and a shell of nanodomains, similar to previous reports in BF-BT-based ceramics. [51, 56, 74-76]

The grain size for BF-BT-xBLN ceramics decreases from  $\sim 8.2 \pm 0.5 \mu\text{m}$  for  $x=0.00$  to  $1.1 \pm 0.2 \mu\text{m}$  for  $x=0.05$  and then increases slightly to  $2 \pm 0.2 \mu\text{m}$  for  $x=0.15$ . The grain size for the optimized composition, BF-BT-0.13BLN, is  $1.5 \pm 0.2 \mu\text{m}$ . The major change in grain size therefore, occurs between  $0 < x < 0.05$ . A sudden decrease in grain size with dopants is common in solid solutions and may be attributed to an increase of grain boundary drag, related to the incorporation of a high valence species such as Nb. [47, 48, 77, 78] The similar grain size for all subsequent compositions for  $x > 0.05$  indicates that it is not a critical factor in optimising the energy density in ceramics as  $x$  increases. However, for multilayers with  $\sim 8 \mu\text{m}$  layer thickness the decrease from  $\sim 8$  to  $\sim 1-2 \mu\text{m}$  is important as it ensures that there are multiple rather than a single grains separating the electrodes and thereby eliminating the potential of short circuit conduction pathways and maintaining a high BDS.

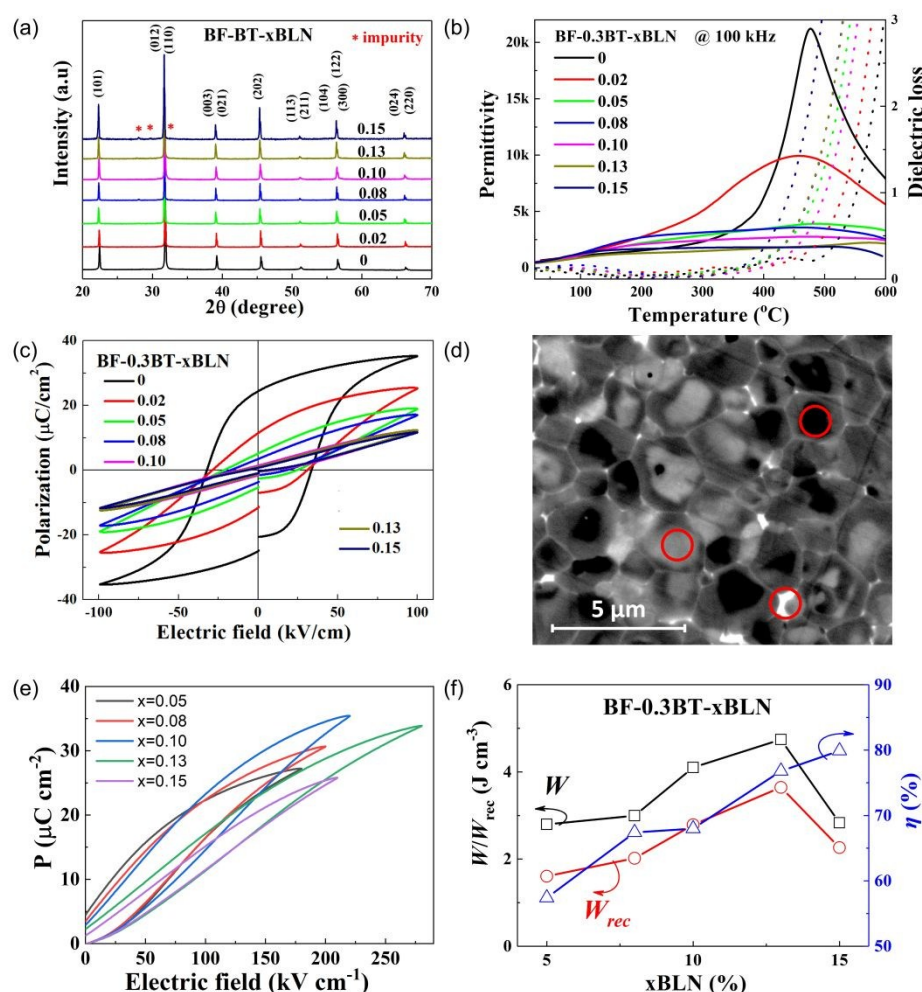


Figure 2. (a) XRD patterns for BF-BT-xBLN ( $x=0.00-0.15$ ). (b) Temperature-dependent permittivity and dielectric loss data for BF-BT-xBLN ceramics at a frequency of 100 kHz. (c) Bipolar P-E loops for BF-BT-xBLN ceramics (d) EDS elemental spot analysis for BF-BT-0.13BLN ceramics. (e) Unipolar P-E loops under  $E_{\max}$  and (f) Energy storage properties under  $E_{\max}$  for BF-BT-xBLN ceramics.

Energy storage properties are obtained using unipolar P-E loops up to the maximum electric field ( $E_{\max}$ ). Due to low BDS ( $<120 \text{ kV cm}^{-1}$ ) and high energy loss, compositions with  $x \leq 0.02$  (Figure 2c) were not considered desirable for energy storage applications. Compositions with  $0.05 \leq x \leq 0.15$  with a strong core-shell contrast exhibits greater potential for energy storage and are considered for further characterization. The unipolar P-E loops of BF-BT-xBLN ( $0.05 \leq x \leq 0.15$ ) under  $E_{\max}$  are displayed in Figure 2e and Figure S9 (Electronic Supplementary Information), with corresponding values of  $P_{\max}$ ,  $P$ ,  $\Delta P$  and  $E_{\max}$  given in Figure S10 (Electronic Supplementary Information). With increasing electric field,  $P_{\max}$  and  $\Delta P$  increase linearly with a slight improvement of  $P_r$  (Figure S10a-e, Electronic Supplementary Information).  $\Delta P$  and  $E_{\max}$  increase initially and then decrease after reaching a maximum of  $\Delta P \sim 32.5 \text{ } \mu\text{C cm}^{-2}$  for  $x=0.10$  and  $E_{\max} \sim 260 \text{ kV cm}^{-1}$  for  $x=0.13$ , respectively (Figure S10f, Electronic Supplementary Information).  $W$ ,  $W_{\text{rec}}$  and  $\eta$  at different electric fields are calculated according to Equations 1-3 and presented in Figure S11 (Electronic Supplementary Information). At  $E_{\max}$ , the highest  $W$  ( $4.74 \text{ J cm}^{-3}$ ) and  $W_{\text{rec}}$  ( $3.64 \text{ J cm}^{-3}$ ) are obtained for  $x = 0.13$  ceramics, while the highest  $\eta$  ( $\sim 80\%$ ) is attained for  $x = 0.15$  ceramics, as illustrated in Figure 2f.

The electrical microstructure of BF-BT-xBLN are investigated by IS as a function of temperature and frequency. The spectroscopic plots of  $Z''$  and  $M''$  at  $250 \text{ }^\circ\text{C}$  for BF-BT-xBLN with  $x=0.00$  and  $x=0.13$  are shown in Figure 3. For undoped BF-BT, two electrical components are observed in the  $M''$  spectra with capacitances ( $C$ ) of  $\sim 6.83 \times 10^{-10}$  and  $1.24 \times 10^{-9} \text{ F cm}^{-1}$ , at 80 Hz and 10 kHz (Figure 3a), respectively. These peaks were temperature dependent, both decreasing in height (and therefore increased in capacitance, as shown in Figure S4, electronic supplementary information) with increasing temperature in the range  $\sim 250 - 400 \text{ }^\circ\text{C}$ . This is consistent with the  $\epsilon_r$ -T data in this range, Figure 2 (a), and indicates that both elements are consistent with ferroelectric-type regions below  $T_c$ . The  $C$  values obtained from the  $M''$  peaks in the spectra are consistent with bulk-type responses for these polar ceramics and the large separation in their  $f_{\max}$  values indicate components with a large difference in resistance ( $R$ ), therefore suggesting the grains are electrically inhomogeneous. Equivalent circuit-fitting (to a first approximation) to a model based on two parallel Resistor-Capacitor (RC) elements connected in series gave plausible temperature-dependent permittivity and conductivity values (see Supplementary Information, Figures S4 and S12, respectively) that are consistent with a conductive-core and resistive-shell type electrical microstructure. A resistivity of  $\sim 1.9 \text{ M}\Omega \text{ cm}$  is obtained from the  $Z''$ - $f$  spectroscopic plot for the lower frequency (shell) component at  $\sim 80 \text{ Hz}$  which dominates the  $Z''$ - $f$  spectrum; an accurate estimate for the resistivity of the higher frequency (core) component cannot be obtained from the  $Z''$ - $f$  spectrum but is calculated to be  $\sim 1.3 \text{ k}\Omega \text{ cm}$  using the relationship  $\omega RC=1$



(where  $\omega=2\pi f$ , with  $f$  in Hz) from the second, higher frequency  $M''$  peak at 10 kHz.<sup>[56, 62]</sup> With increasing BLN concentration, the higher frequency  $M''$  peak associated with the core-type response remains clearly visible for  $x < 0.08$ ; however, for  $0.08 \leq x \leq 0.15$  its presence has visibly decreased and is absent for  $x \geq 0.13$ , Figure S13 and S14 (Electronic Supplementary Information). The large  $Z''$  spectroscopic peak remains at  $\sim 100$  Hz with increasing BLN content, however its magnitude increases from  $\sim 2$  to  $3$  M $\Omega$  cm, Figure S13 (Electronic Supplementary Information).

Only a single peak is observed in the spectroscopic plots of  $Z''$  and  $M''$  at 250 °C for  $x=0.13$  (Figure 3b), corresponding to a single bulk component with  $C \sim 1.68 \times 10^{-10}$  F cm $^{-1}$  (from the  $M''$  peak) and resistivity,  $R$  of  $\sim 6$  M $\Omega$  cm (from the  $Z''$  peak). It is noteworthy that the  $M''$  peak height is largely invariant in the temperature range  $\sim 250 - 400$  °C (Figure 3d) which is consistent with the flat  $\epsilon_r$ - $T$  response observed from fixed frequency dielectric measurements in Figure 2 (b). Temperature-dependent spectroscopic plots of  $M''$  for  $x=0.00$  and  $x=0.13$  are displayed in Figure 3c and d. The high-frequency conductive component observed for  $x=0.00$  can only be observed below 350 °C due to its time constant (RC product) exceeding the upper frequency range measured in our experiments. All  $M''$  peaks for  $x=0.00$  and  $x=0.13$  shift to higher frequency with increasing temperature with their peak heights and confirms the predominantly ferroelectric nature of core and shell components in  $x = 0$  and overall relaxor-ferroelectric behaviour in the electrically homogeneous grains of  $x = 0.13$ . The IS data indicates that short circuit conduction paths are more likely to form under high field for  $x < 0.08$  via the conductive grain cores, however, for  $x > 0.08$ , enhanced BDS as well as energy density can be achieved due to improved electrical homogeneity with a much lower volume fraction of conductive cores.

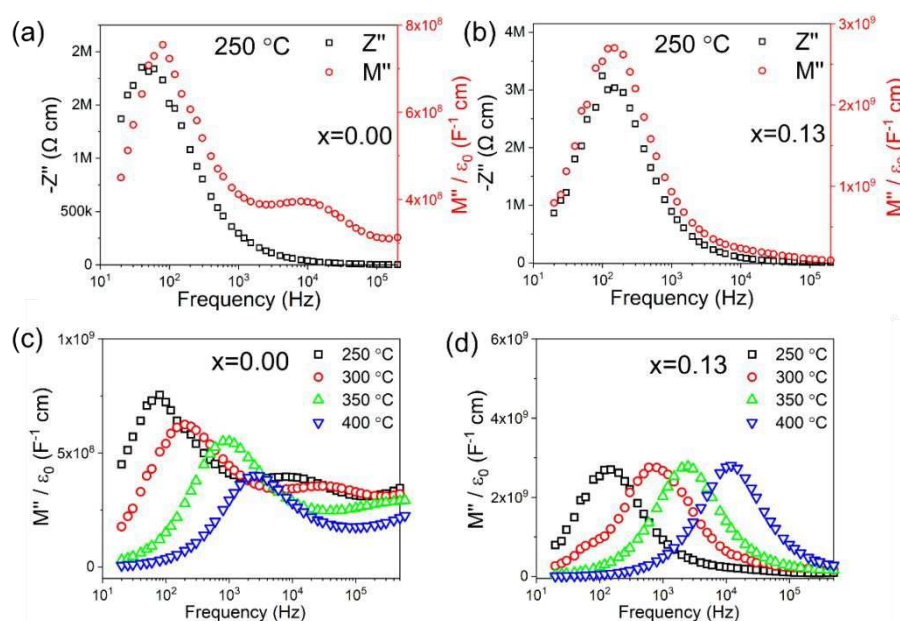


Figure 3. Combined  $Z''$  and  $M''$  spectroscopic plots at 250 °C for  $x=(a)$  0.00 and  $(b)$  0.13; Temperature-dependent  $M''$  spectroscopic plots for  $x=(c)$  0.00 and  $(d)$  0.13.



## Multilayer ceramic capacitors (MLCCs)

View Article Online  
DOI: 10.1039/D0TA00216J

To increase the BDS and energy storage properties, multilayer ceramic capacitors of BF-BT-0.13BLN were fabricated with  $\sim 8 \mu\text{m}$  thick dielectric layers with active electrode area of  $5 \text{ mm}^2$ , as presented in Figure 4 (a, b).

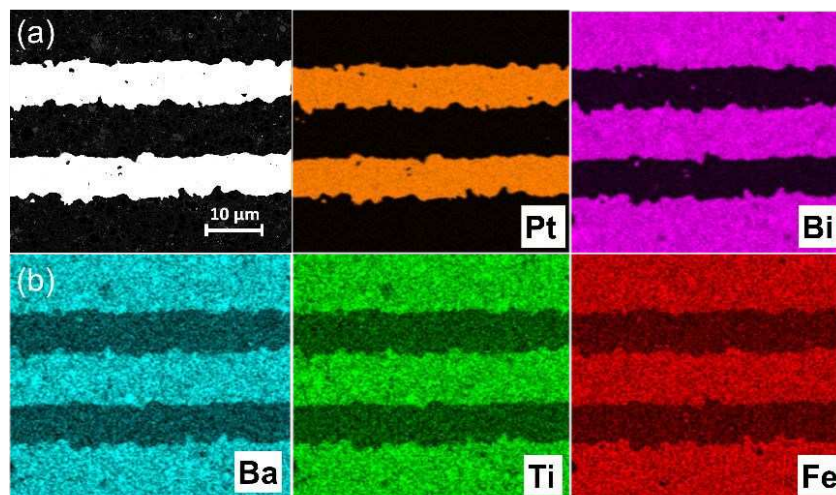


Figure 4. (a) BSE cross section micrographs of BF-BT-13BLN multilayer MLCCs; (b) EDX mapping of each elemental metal distribution.

Figure 5(a) shows a TEM image obtained from the interface between the BF-BT-13BLN ceramic and Pt electrode. According to the selected area electron diffraction (SAED) patterns in Figure 5(b) and 5(c), the  $\{001\}$  atomic planes of the ceramic grain displayed in Figure 5(a) are  $\sim 4^\circ$  off parallel to Pt $\{115\}$  but we do not suggest that this is due an epitaxial relation as the multilayers are formed by a powder-based tape-cast process. Consistent with XRD results, the SAED patterns displayed in Figure 5b and Figure S15 (Electronic Supplementary Information) obtained from the BF-BT-13BLN ceramic along  $[210]$  and  $[100]$  zone axes, respectively, indicating they are perovskite structured. An amorphous layer ( $\sim 4 \text{ nm}$ ) is observed at the interface between the Pt and the ceramic. The role of the amorphous layer is not detrimental to energy storage properties and may have a positive effect on breakdown strength through moderating field concentrations at the electrode/dielectric interface and on polarization through a space-charge mechanism. According to EDS elemental maps presented in Figure 5d, the amorphous layer is rich in Ba, Ti and Fe but deficient in Bi. Bi however, is present at the surface of the Pt. Similar amorphous layers have been reported in BT-based MLCCs and their formation attributed to binder (Carbon-related) burnout during the sintering process.<sup>[34]</sup> Potentially this layer can be suppressed by slower or longer binder burnout stages during sintering of the devices.



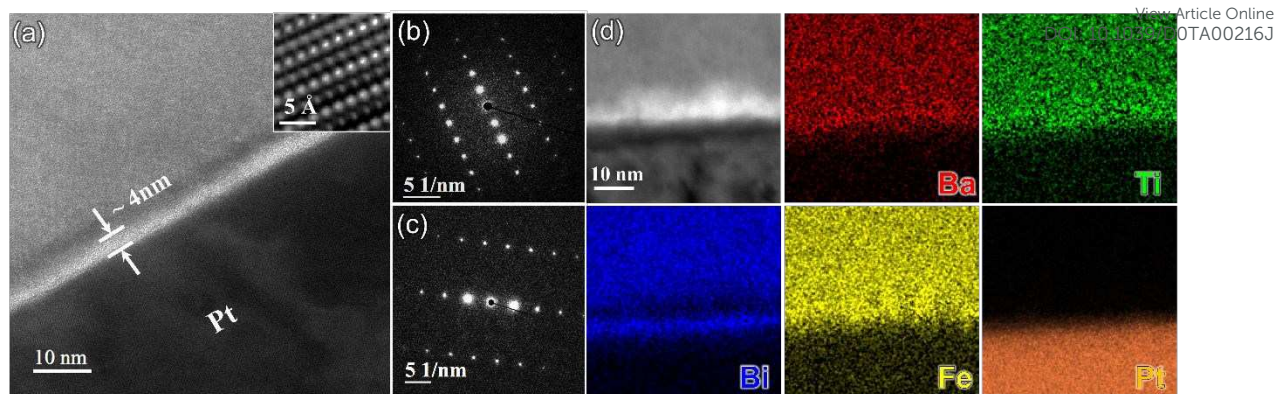


Figure 5. (a) TEM micrograph obtained from an interface between a BF-BT-13BLN grain and a Pt grain (electrode). Here the Pt grain is close to its [321] zone axis and the BF-BT-13BLN grain is  $\sim 4^\circ$  off from its [210] zone axis; inset shows an HRTEM image (filtered) obtained from the BF-BT-13BLN grain at a higher magnification. (b)  $\langle 210 \rangle$  SAED pattern obtained from the BF-BT-13BLN grain displayed in (a). (c)  $\langle 321 \rangle$  SAED pattern obtained from the Pt grain displayed in (a). (d) Bright field STEM image and corresponding chemical EDX maps obtained from an interface between a BF-BT-13BLN grain and a Pt grain (electrode).

We conclude that Bi is reduced at the Pt/dielectric interface by residual carbon from the binder. The reduction of Bi is enhanced by the formation of an alloy with the Pt, driven by the increase in entropy (reduction in free energy) through mixing. The unipolar P-E loops and energy storage properties of BF-BT-13BLN multilayers, are shown in Figure 6(a-b).  $P_{max} \sim 52 \mu\text{C cm}^{-2}$  and  $P_r \sim 4 \mu\text{C cm}^{-2}$ , are obtained for multilayers at  $953 \text{ kV cm}^{-1}$ . The energy storage properties of multilayers are significantly enhanced with respect to monolithic ceramics, yielding a record-high  $W_{rec} = 13.8 \text{ J cm}^{-3}$  with  $\eta = 81\%$  at  $953 \text{ kV cm}^{-1}$ ; the highest value to date for lead/lead-free ceramics and multilayers (Figure 6 c-d and Table S3, Electronic Supplementary Information), fabricated using a scalable powder based technology.



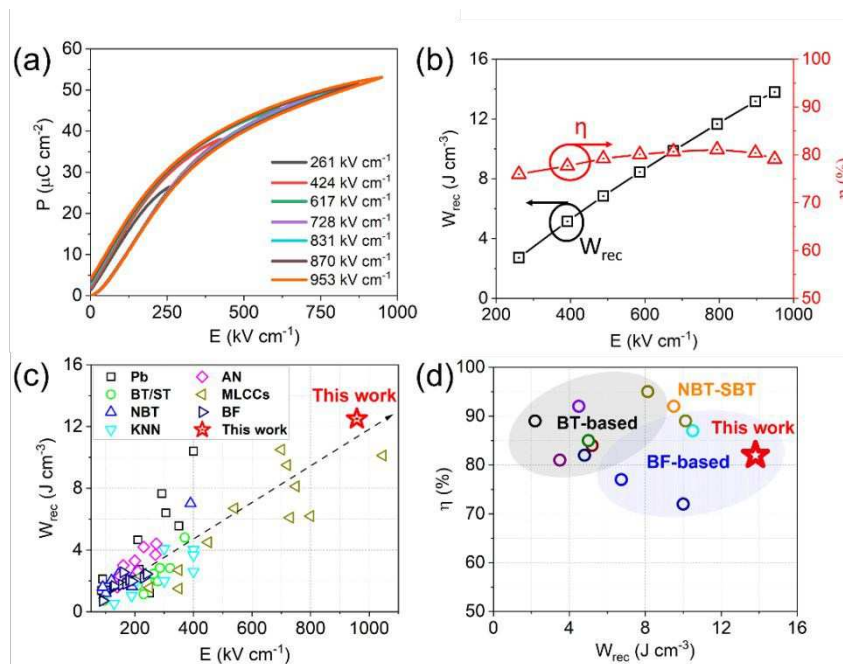


Figure 6. (a) RT Unipolar P-E loops and (b) Calculated energy storage properties for BF-BT-13BLN multilayers. (c) Comparison of  $W_{\text{rec}}$  vs. electric field for different lead/lead-free bulk ceramics and multilayers. [24-56, 79-99] (d) Comparison of  $W_{\text{rec}}$  vs.  $\eta$  for lead-free multilayers. [31, 33-35, 43, 51, 56, 99, 100]

The unipolar P-E loops and energy storage properties ( $W_{\text{rec}}$  and  $\eta$ ), obtained from 25 to 100 °C, from 0.01 to 100 Hz and cycled up to  $10^4$  times at 400  $\text{kV cm}^{-1}$  are shown in Figure 7.  $W_{\text{rec}}$  is temperature stable (< 10%) from 25 to 100 °C, with little variation (<5%) as a function of frequency from 0.01 to 100 Hz and cyclic poling up to  $10^4$  times.

There are many factors which influence the excellent properties of these materials. The high value of  $W_{\text{rec}}$  is a direct consequence of being able to apply a large electric field without breakdown to a material whose crystal chemistry is designed to house highly polarisable ions within a matrix of dissimilar sized  $\text{ABO}_3$  perovskite unit cells (enhanced local polarisability). [59] Temperature stability is still limited mainly by the conductivity mechanisms which become active under high electric field. In BF-BT based ceramics,  $\text{V}_\text{O}$  diffusion is facilitated above 100 °C at high electric field and creates loss, widening the unipolar loop and reducing efficiency. Nonetheless, in comparison to polymer-based capacitors with similar energy densities, the materials show promise for high-temperature applications. Our multilayers exhibit negligible degradation after  $10^4$  cycles of the unipolar P-E loops, possibly due to the absence of significant strain ( $S < 0.03\%$ ) at 400  $\text{kV cm}^{-1}$ . Excellent fatigue properties are often associated with relaxor-like compositions, particular ones whose permittivity maximum is suppressed through doping with a third end member. [32, 33, 51]. The low strain prevents large cyclic changes in dimensions and eventual micro-cracking. Lead-based bulk ceramic or ceramic films, often exhibit excellent energy storage performance but are accompanied by high electric field-induced strain ( $S > 0.4\%$ ), leading to thermo- and mechanical-related failure due to micro-cracking. [101-103]



Multilayers with  $x = 0.13$  therefore, have the potential to replace the lead-based systems for pulsed power applications. Furthermore, BT-BF-13BLN multilayers are rare-earth (RE)-free with low sintering temperature  $\sim 890$  °C, providing an opportunity for sustainable manufacturing and indicating potential compatibility with Ag-10%Pd internal electrodes.

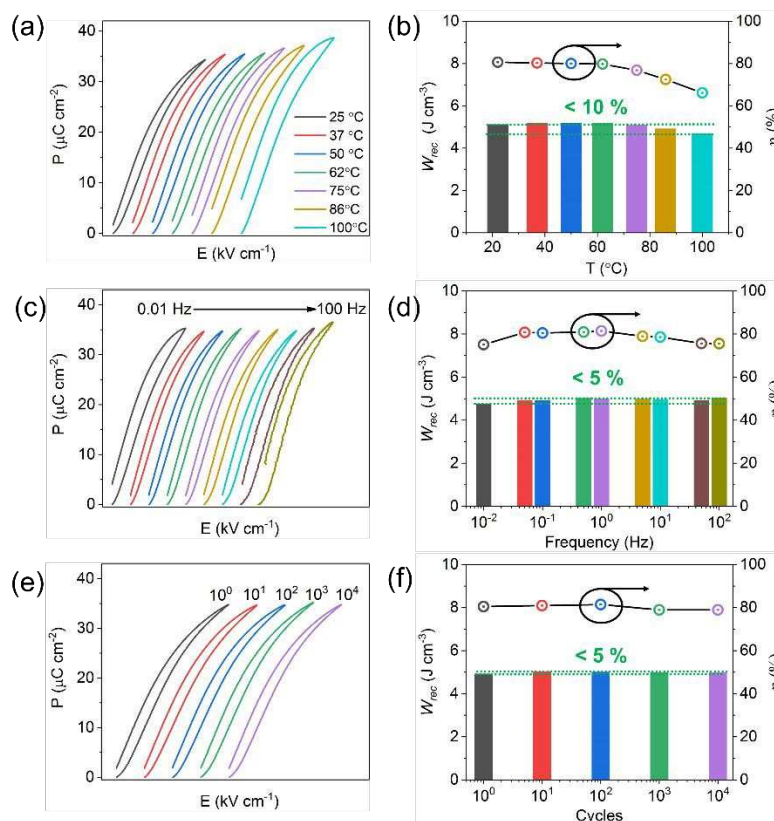


Figure 7. (a) Unipolar P-E loops at temperature range from 25 to 100 °C and (b) calculated energy storage properties at 400  $\text{kV cm}^{-1}$ ; (c) unipolar P-E loops at frequency range from 0.01 to 100 Hz and (d) calculated energy storage properties at 400  $\text{kV cm}^{-1}$ ; (e) unipolar P-E loops cycled up to  $10^4$  times and (f) calculated energy storage properties for BF-BT-13BLN multilayers at 400  $\text{kV cm}^{-1}$ .

## Conclusions

In summary, novel  $(0.7-x)\text{BiFeO}_3-0.30\text{BaTiO}_3-x\text{Bi}(\text{Li}_{0.5}\text{Nb}_{0.5})\text{O}_3$  (BF-BT-xBLN) ceramics and multilayers are successfully fabricated using solid-state reaction and tape-casting, respectively.  $W_{rec} \sim 13.8$   $\text{J cm}^{-3}$  was recorded at 953  $\text{kV cm}^{-1}$  for multilayers with  $\sim 8$   $\mu\text{m}$  thick dielectric layers. Under electric field of 400  $\text{kV cm}^{-1}$ , multilayers are temperature stable ( $<10\%$ ) from RT to 100 °C, frequency independent ( $<5\%$ ) from 0.01 to 100 Hz and fatigue-resistant ( $<5\%$ ) up to  $10^4$  cycles of the unipolar P-E loops. Additionally, BT-BF-13BLN multilayers are rare earth-free with a low sintering temperature (890 °C) and are therefore considered promising lead-free candidates for energy storage applications.



## Materials and Methods

### Ceramics and MLCCs fabrication

BF-BT based ceramics within the ternary solid solution,  $(0.7-x)\text{BiFeO}_3\text{-}0.3\text{BaTiO}_3\text{-}x\text{Bi}(\text{Li}_{1/2}\text{Nb}_{1/2})\text{O}_3$  (BF-BT-xBLN,  $x = 0.00, 0.02, 0.5, 0.08, 0.10, 0.13, 0.15$ ) were synthesized using conventional solid-state reaction.<sup>[51, 52]</sup> Ceramic multilayers were fabricated using an MTI MSK-AFA-II tape caster with a single doctor blade on a single-side silicon-coated mylar film. Pt electrodes were printed onto the tape using a DEK 247 screen printer, followed by tape stacking and hot-pressing (70 °C for 10 mins). Multilayers were sintered at 890 °C for 2 h with an intermediate binder burnout step (180 °C for 4h and 300 °C for 2h). Finally, Au terminal electrodes were painted on the side of the multilayers and fired 2 h at 850 °C.<sup>[56]</sup>

### Microstructural Characterization

Densities of sintered ceramics were determined by the Archimedes method and achieved >95% of the theoretical density. The phase assemblage, structure and microstructure at room temperature (RT) were evaluated by X-ray powder diffraction (XRD, Bruker D2 Phaser) and scanning electron microscopy (SEM, FEI Inspect F50 equipped with a backscattered (BSE) detector). For SEM, sintered samples were firstly ground then polished to a mirror finish using wet abrasive paper and diamond paste (MetPrep Ltd.). Specimens for transmission electron microscopy (TEM) were prepared by mechanical grinding, polishing and then ion milling. Ion milling was performed using a Gatan precision ion polishing system (PIPS II) at liquid nitrogen temperature to minimize surface damage of the specimens. A JEOL-F200 microscope was used for high resolution transmission electron microscopy (HRTEM) and scanning transmission electron microscopy (STEM) imaging as well as energy dispersive X-ray (EDX) spectroscopy analysis.

### Electrical Characterization

For electrical measurements, Au was sputtered on the top and bottom surfaces of ceramic pellets. Ferroelectric polarization-electric field (P-E) was measured using an aixACCT TF 2000E system from RT to 125 °C using a 1 Hz triangular signal. The dielectric properties as a function of temperature were evaluated from RT to 600 °C at 1, 10, 100 and 250 kHz using an LCR meter (Agilent 4184A). Impedance data were collected using an Agilent E4980A impedance AC analyser from RT to 400 °C at intervals of 25 °C. Impedance data were normalised by a geometric factor (thickness/surface area) and then analyzed using a ZView software (Scribner Associates, Inc., Southern Pines, NC). Details of how Resistance and Capacitance values were extracted for the different electro-active regions from combined  $Z''$  and  $M''$  spectroscopic plots are given in a previous publication.<sup>[68, 104, 105]</sup>

### CONFLICT OF INTERESTS



The authors declare no competing financial interest.

View Article Online  
DOI: 10.1039/D0TA00216J

## ACKNOWLEDGMENT

This work was supported by the Engineering and Physical Sciences Research Council (EP/L017563/1 and EP/N010493/1), Henry Royce Institute for Advanced Materials, funded through EPSRC grants EP/R00661X/1, EP/S019367/1, EP/P02470X/1 and EP/P025285/1 and National Natural Science Foundation of China (51602060 and 51402005). The authors are grateful for support provided by Functional Materials and Devices group from University of Sheffield and would like to thank Zhongming Fan from Iowa State University for assistance with TEM work.



## References

- [1] B. Chu, X. Zhou, K. Ren, B. Neese, M. Lin, Q. Wang, F. Bauer, Q. M. Zhang, *Science*. 2006, **313**, 334-336.
- [2] Q. Li, L. Chen, M. R. Gadinski, S. Zhang, G. Zhang, H. Li, A. Haque, L. Chen, T. Jackson, Q. Wang, E. Iagodkine, *Nature*, 2015, **523**, 576-579.
- [3] L. Zhao, Q. Liu, J. Gao, S. Zhang, J. F. Li, *Adv. Mater.* 2017, **29**, 1701824-7.
- [4] G. R. Love, *J. Am. Ceram. Soc.* 1990, **73**, 323-328.
- [5] K. Seongtae, W. Hackenberger, E. Alberta, E. Furman, M. Lanagan, *IEEE Electr. Insul. Mag.* 2011, **27**, 43-55.
- [6] H. Sun, W. Wang, H. Jiao, S. Wang, H. Zhu, S. Jiao, *ChemComm.*, 2015, **51**, 11892-11895.
- [7] X. Zhang, S. Jiao, J. Tu, W-L. Song\*, X. Xiao, S. Li, M. Wang, H. Lei, D. Tian, H. Chen, D. Fang, *Energy Environ. Sci.*, 2019, **12**, 1918-1927.
- [8] S. Wang, S. Jiao, J. Wang, H-S. Chen, D. Tian, H. Lei, and D-N. Fang, *ACS Nano*, 2017, **11**, 467-477.
- [9] Z. Yu, S. Jiao, S. Li, X. Chen, W-L. Song\*, T. Teng, J. Tu, H-S. Chen, G. Zhang, D-N. Fang, *Adv. Funt. Mater.*, 2019, **29**, 1806799.
- [10] Y. Song, S. Jiao, J. Tu, J. Wang, Y. Liu, H. Jiao, X. Mao, Z. Guo, D. J. Fray. *J. Mater. Chem. A*, 2017, **5**, 1282-1291.
- [11] H. Jiao, C. Wang, J. Wang, J. Tu, J. Zhu, S. Jiao, *ChemComm.*, 2017, **53**, 2331-2334.
- [12] S. Wang, Z. Yu, J. Tu, J. Wang, D. Tian, Y. Liu, S. Jiao, *Adv. Energy Mater.*, 2016, **6**, 1600137.
- [13] W. Wang, B. Jiang, W. Xiong, H. Sun, Z. Lin, L. Hu, J. Tu, J. Hou, H. Zhu, S. Jiao, *Sci. Rep.*, 2013, **3**, 3383.
- [14] W. B. Hu, Y. Liu, R. L. Withers, T. J. Frankcombe, L. Noren, A. Snashall, M. Kitchin, P. Smith, B. Gong, H. Chen, J. Schiemer, F. Brink, J. Wong-Leung, *Nat. Mater.* 2013, **12**, 821-826.
- [15] Q. Li, G. Zhang, F. Liu, K. Han, M. R. Gadinski, C. Xiong, Q. Wang, *Energy Environ. Sci.* 2015, **8**, 922-931.
- [16] C. Liu, F. Li, L. P. Ma, H. M. Cheng, *Adv. Mater.* 2010, **22**, E28-E62.
- [17] I. Hadjipaschalis, A. Poullikkas, V. Efthimiou, *Renewable Sustainable Energy Rev.* 2009, **13**, 1513-1522.
- [18] H. Chen, T. N. Cong, W. Yang, C. Tan, Y. Li, Y. Ding, *Prog. Nat. Sci.* 2009, **19**, 291-312.
- [19] Z. Fan, C. Zhou, X. Ren, X. Tan, *Appl. Phys. Lett.* 2017, **111**, 252902.
- [20] Z. Fan, J. Koruza, J. Rodel, X. Tan, *Acta. Mater.* 2018, **151**, 253-259.
- [21] Z. Fan, X. Tan, *J. Eur. Ceram. Soc.* 2018, **38**, 3472-3477.
- [22] Z. Fan, L. Zhou, T. H. Kim, J. Zhang, S. T. Zhang, X. Tan, *Phys. Rev. Mater.* 2019, **3**, 024402.



- [23] H. Wang, Y. Liu, T. Yang, S. Zhang, *Adv. Funct. Mater.* 2019, **29**, 1807321.
- [24] L. Zhao, Q. Liu, S. Zhang, J-F, Li, *J. Mater. Chem. A.* 2016, **4**, 8380.
- [25] Y. Tian, L. Jin, H. Zhang, Z. Xu, X. Wei, E. D. Politova, S. Y. Stefanovich, N. V. Tarakina, I. Abrahams, H. Yan, *J. Mater. Chem. A.* 2016, **4**, 17279.
- [26] L. Zhao, J. Gao, Q. Liu, S. Zhang, J-F, Li, *ACS Applied Materials and interfaces.* 2018, **10**, 819-826.
- [27] L. Zhao, Q. Liu, J. Gao, S. Zhang, J-F, Li, *Adv. Mater.* 2017, **29**, 1701824.
- [28] Y. Tian, L. Jin, H. Zhang, Z. Xu, X. Wei, G. Viola, I. Abrahams, H. Yan, *J. Mater. Chem. A.* 2017, **5**, 17525.
- [29] Q. Yuan, G. Li, F-Z. Yao, S-D. Cheng, Y. Wang, R. Ma, S-B. Mi, M. Gu, K. Wang, J-F. Li, H. Wang, *Nano Energy.* 2018, **52**, 203-210.
- [30] Q. Fan, M. Liu, C. Ma, L. Wang, S. Ren, L. Lu, X. Lou, C-L. Jia, *Nano Energy.* 2018, **51**, 539-545.
- [31] W-B. Li, D. Zhou, R. Xu, L-X. Pang, I. M. Reaney, *ACS Appl. Energy Mater.* 2018, **1**, 5016-5023.
- [32] W-B. Li, D. Zhou, L-X. Pang, R. Xu, H-H. Guo, *J. Mater. Chem. A.* 2017, **5**, 19607-19612.
- [33] W. Li, D. Zhou, R. Xu, D-W. Wang, J. Su, L-X. Pang, W. Liu, G-H. Chen, *ACS Appl. Energy Mater.* 2019, **2**, 5499-5506.
- [34] Z. Cai, C. Zhu, H. Wang, P. Zhao, L. Chen, L. Li, X. Wang, *J. Mater. Chem. A.* 2019, **7**, 14575.
- [35] P. Zhao, H. Wang, L. Wu. L. Chen, Z. Cai, L. Li, X. Wang, *Adv. Energy. Mater.* 2019, **9**, 1803048.
- [36] Z. Shen, X. Wang, B. Luo, L. Li, *J. Mater. Chem. A.* 2015, **3**, 18146.
- [37] H. Qi, R. Zuo, *J. Mater. Chem. A.* 2019, **7**, 3971.
- [38] Y. Pu, L. Zhang, Y. Cui, M. Chen, *ACS Sustainable Chem. Eng.* 2018, **6**, 6102-6109.
- [39] J. Wu, A. Mahajan, L. Riekehr, H. Zhang, B. Yang, N. Meng, Z. Zhang, H. Yan, *Nano Energy.* 2018, **50**, 723-732.
- [40] H. Yang, F. Yan, Y. Lin, T. Wang, *ACS Sustainable Chem. Eng.* 2017, **5**, 10215-10222.
- [41] Z. Pan, D. Hu, Y. Zhang, J. Liu, B. Shen, J. Zhai, *J. Mater. Chem. C.* 2019, **7**, 4072-4078.
- [42] C. Yang, P. Lv, J. Q, Y. Han, J. Ouyang, X. lin, S. Huang, Z. Cheng, *Adv. Energy. Mater.* 2019, **9**, 1803949.
- [43] J. Li, F. Li, Z. Xu, S. Zhang, *Adv. Mater.* 2018, **30**, 1802155.
- [44] Y. Zhang, W. Li, S. Xu, Z. Wang, Y. Zhao, J. Li, W. Fei, *J. Mater. Chem. A.* 2018, **6**, 24550-24559.
- [45] F. Li, J. Zhai, B. Shen, X. Liu, H. Zeng, *Mater. Res. Lett.* 2018, **6**, 345-352.
- [46] B. Qu, H. Du, Z. Yang, Q. Liu, T. Liu, *RSC Adv.* 2016, **6**, 34381.
- [47] Z. Yang, H. Du, S. Qu, Y. Hou, H. Ma, J. Wang, J. Wang, X. Wei, Z. Xu, *J. Mater. Chem. A.* 2016, **4**, 13778.
- [48] T. Shao, H. Du, H, Ma, S. Qu, J. Wang, J. Wang, X. Wei, Z. Xu, *J. Mater. Chem. A.* 2017, **5**, 554.

View Article Online  
DOI: 10.1039/D0TA00216J



- [49] B. Qu, H. Du, Z. Yang, Q. Liu, *J. Am. Ceram. Soc.* 2017, **100**, 1517-1526.
- [50] D. Wang, Z. Fan, W. Li, D. Zhou, A. Feteira, G. Wang, S. Murakami, S. Sun, Q. Zhao, X. Tan, I. M. Reaney, *ACS Appl. Energy Mater.* 2018, **1**, 4403-4412.
- [51] D. Wang, Z. Fan, D. Zhou, A. Khesro, S. Murakami, A. Feteira, Q. Zhao, X. Tan, I. M. Reaney, *J. Mater. Chem. A*. 2018, **6**, 4133.,
- [52] D. Zheng, R. Zuo, D. Zhang, Y. Li, *J. Am. Ceram. Soc.* 2015, **98**, 2692-2695.
- [53] D. Zheng, R. Zuo, *J. Eur. Ceram. Soc.* 2017, **37**, 413-418.
- [54] N. Liu, R. Liang, X. Zhao, C. Xu, Z. Zhou, X. Dong, *J. Am. Ceram. Soc.* 2018, **101**, 3259-3265.
- [55] D. Wang, G. Wang, S. Murakami, Z. Fan, A. Feteira, D. Zhou, S. Sun, Q. Zhao, I. M. Reaney, *J. Adv. Dielectrics*, 2018, **8**, 1830004.
- [56] G. Wang, J. Li, X. Zhang, Z. Fan, F. Yang, A. Feteira, D. Zhou, D. C. Sinclair, T. Ma, X. Tan, D. Wang, I. M. Reaney, *Energy Environ, Sci.* 2019, **12**, 582.
- [57] M. H. Lee, D. J. Kim, J. S. Park, S. W. Kim, T. K Song, M-H. Kim, W-J. Kim, D. Do, I-K, Jeong, *Adv. Mater.* 2015, **27**, 6976.
- [58] G. H. Ryu, A. Hussain, M. H. Lee, R. A. Malik, T-K Song, W-J. Kim, M-H. Kim, *J. Eur. Ceram. Soc.* 2018, **38**, 4414-4421.
- [59] I. Lewin, W. J. Laws, D. Wang, I. M. Reaney, *Appl. Phys. Lett.* 2017, **111**, 212902.
- [60] P. Fiorenza, R. L. Nigro, P. Delugas, V. Raineri, A. G. Mould, D. C. Sinclair, *Appl. Phys. Lett.*, 2009, **95**, 142904.
- [61] J. P. Heath, J. H. Harding, D. C. Sinclair, J. S. Dean, *Adv. Funct. Mater.*, 2019, **29**, 1904036.
- [62] J. T. S. Irvine, D. C. Sinclair, A. R. West, *Adv. Mater.* 1990, **2**, 132-138.
- [63] L. Yang, X. Kong, F. Li, H. Hao, Z. Cheng, H. Liu, J-F. Li, S. Zhang, *Prog. Mater. Sci.* 2019, **102**, 72-108.
- [64] R. Gerson, T. C. Marshall, *J. Appl. Phys.* 1959, **30**, 1650.
- [65] H. Pan, F. Li, Y. Liu, Q. Zhang, M. Wang, S. Lan, Y. Zheng, J. Ma, L. Gu, Y. Shen, P. Yu, S. Zhang, L-Q. Chen, Y-H. Lin, C-W. Nan, *Science*, 2019, **365**, 578-582.
- [66] F. Yang, M. Li, L. Li, P. Wu, E. Pradal-Velazquez, D. C. Sinclair, *J. Mater. Chem. A*, 2018, **6**, 5243-5254.
- [67] M. Li, L. Li, J. Zang, D. C. Sinclair, *Appl. Phys. Lett.*, 2015, 106, 102904.
- [68] L. Li, M. Li, H. Zhang, I. M. Reaney, D. C. Sinclair, *J. Mater. Chem. C*, 2016, **4**, 5779-5786.
- [69] A. Khesro, D. Wang, F. Hussain, D. C. Sinclair, A. Feteira, I. M. Reaney, *Appl. Phys. Lett.*, 2016, **109**, 142907.
- [70] S. Murakami, D. Wang, A. Mostaed, A. Khesro, A. Feteira, D. C. Sinclair, Z. Fan, X. Tan, I. M. Reaney, *J. Am. Ceram. Soc.* 2018, **101**, 5428-5442.
- [71] S. Murakami, N. T. A. F. Ahmed, D. Wang, A. Feteira, D. C. Sinclair, I. M. Reaney, *J. Eur. Ceram. Soc.* 2018, **38**, 4220-4231.



- [72] R. D. Shannon, *Acta Crystallogr., Sect. A.* 1976, **32**, 751.
- [73] G. Wang, Z. Fan, S. Murakami, Z. Lu, D. A. Hall, D. C. Sinclair, A. Feteira, X. Tan, J. L. Jones, A. K. Kleppe, D. Wang, I. M. Reaney, *J. Mater. Chem. A.* 2019, **7**, 21254-21263.
- [74] I. Calisir, A. K. Kleppe, A. Feteira, D. A. Hall, *J. Mater. Chem. C.* 2019, **7**, 10218-10230.
- [75] I. Calisir, A. A. Amirov, A. K. Kleppe, D. A. Hall, *J. Mater. Chem. A.* 2018, **6**, 5378-5397.
- [76] I. Calisir, D. A. Hall, *J. Mater. Chem. C.* 2018, **6**, 134-146.
- [77] Y. Lin, D. Li, M. Zhang, S. Zhan, Y. Yang, H. Yang, Q. Yuan, *ACS Appl. Mater. Interfaces*, 2019, **11**, 36824-36830.
- [78] G. Wang, Z. Lu, Z. Zhang, A. Feteira, C. C. Tang, D. A. Hall, *J. Am. Ceram. Soc.*, 2019, **102**, 7746-7754.
- [79] L. Zhang, S. Jiang, B. Fan, G. Zhang, *J. Alloys Compd.* 2015, **622**, 162-165.
- [80] Z. Liu, X. Chen, W. Peng, C. Xu, X. Dong, F. Cao, G. Wang, *Appl. Phys. Lett.* 2015, **106**, 262901.
- [81] Q. Zhang, H. Tong, J. Chen, Y. Lu, T. Yang, X. Yao, Y. He, *Appl. Phys. Lett.* 2016, **109**, 262901.
- [82] R. Xu, B. Li, J. Tian, Z. Xu, Y. Feng, X. Wei, D. Huang, L. Yang, *Appl. Phys. Lett.* 2017, **110**, 142904.
- [83] Q. Zhang, J. Chen, Y. Lu, T. Yang, X. Yao, Y. He, *J. Am. Ceram. Soc.* 2016, **99**, 3853-3856.
- [84] Q. Zhao, H. Lei, G. He, J. Di, D. Wang, P. Tan, H. Jin, H. M. Cao, *Ceram. Int.* 2016, **42**, 1314-1317.
- [85] F. Yan, H. Yang, Y. Lin, T. Wang, *Inorg. Chem.* 2017, **56**, 13510-13516.
- [86] J. Yin, X. Lv, J. Wu, *Ceram. Int.* 2017, **43**, 13541-13546.
- [87] Y. Pu, M. Yao, L. Zhang, M. Chen, *J. Alloys Compd.* 2017, **702**, 171-177.
- [88] H. Tao, J. Wu, *J. Mater. Sci.: Mater. Electron.* 2017, **28**, 16199-16204
- [89] H. Yang, F. Yan, Y. Lin, T. Wang, L. He, F. Wang, *J. Alloys Compd.* 2017, **710**, 436-445.
- [90] H. Yang, F. Yan, Y. Lin, T. Wang, F. Wang, Y. Wang, L. Guo, W. Tai, H. Wei, *J. Eur. Ceram. Soc.* 2017, **37**, 3303-3311.
- [91] H. Yang, F. Yan, Y. Lin, T. Wang, *Appl. Phys. Lett.* 2017, **111**, 253903.
- [92] Q. M. Zhang, L. Wang, J. Luo, Q. Tang, J. Du, *Int. J. Appl. Ceram. Technol.* 2010, **7**, E124-E128.
- [93] Y. H. Huang, Y. J. Wu, Y. J. W. J. Qiu, J. Li, X. M. Chen, *J. Eur. Ceram. Soc.* 2015, **35**, 1469-1476.
- [94] W. B. Li, D. Zhou, L-X. Pang, *Appl. Phys. Lett.* 2017, **110**, 132902-5.
- [95] T. Wang, L. Jin, C. C. Li, Q. Y. Hu, X. Y. Wei, *J. Am. Ceram. Soc.* 2015, **98**, 559-566.
- [96] Q. Y. Hu, L. Jin, T. Wang, C. C. Li, Z. Xing, X. Y. Wei, *J. Alloys Compd.* 2015, **640**, 416-420.
- [97] Q. Xu, J. Xie, Z. C. He, L. Zhang, M. H. Cao, X. D. Huang, M. T. Lanagan, H. Hao, Z. H. Yao, H. X. Liu, *J. Eur. Ceram. Soc.* 2017, **37**, 99-106.
- [98] L. Chen, Y. Li, Q. Zhang, X. Hao, *Ceram. Int.* 2016, **42**, 12537-12542.
- [99] H. Ogihara, C. A. Randall, S. Trolier-McKinstry, *J. Am. Ceram. Soc.* 2009, **92**, 1719-1724.

View Article Online  
DOI: 10.1039/D0TA00216J



- [100] G. Wang, Z. Lu, J. Li, H. Ji, H. Yang, L. Li, S. Sun, A. Feteira, H. Yang, R. Zuo, D. Wang, J. M. Reaney, *J. Eur. Ceram. Soc.*, 2020, **40**, 1779-1783. [View Article Online](#)  
[DOI: 10.1039/D0TA00216J](https://doi.org/10.1039/D0TA00216J)
- [101] Q. Zhang, J. Chen, Y. Lu, T. Yang, X. Yao, Y. He, *J. Am. Ceram. Soc.* 2016, **99**, 3853-3856.
- [102] L. Chen, N. Sun, Y. Li, Q. Zhang, L. Zhang, X. Hao, *J. Am. Ceram. Soc.* 2018, **101**, 2313-2320.
- [103] M. S. Mirshekarloo, K. Yao, T. Sritharan, *Appl. Phys. Lett.* 2010, **97**, 142902.
- [104] L. Li, M. Li, I. M. Reaney, D. C. Sinclair, *J. Mater. Chem. C.* 2017, **5**, 6300-6310.
- [105] L. Li, M. Li, D. C. Sinclair, *Appl. Phys. Lett.* 2018, **112**, 182907.

